doi:10.1006/jmbi.2001.5411 available online at http://www.idealibrary.com on IDEAL® *J. Mol. Biol.* (2002) **317**, 145–158

JMB

Solution Structure of Protein SRP19 of *Archaeoglobus fulgidus* Signal Recognition Particle

Olga N. Pakhomova , Shashank Deep[1], Qiaojia Huang[2] Christian Zwieb[2] and Andrew P. Hinck[1]*

[1]*Department of Biochemistry Center for Biomolecular Structure Analysis, University of Texas Health Science Center at San Antonio, 7703 Floyd Curl Drive, San Antonio TX 78229, USA*

[2]*Department of Molecular Biology, The University of Texas Health Science Center at Tyler, 11937 US Highway 271 Tyler, TX 75708, USA*

**Corresponding author*

Protein SRP19 is an essential RNA-binding component of the signal recognition particle (SRP) in Archaea and Eucarya. A three-dimensional solution structure of the 104 residue SRP19 from the hyperthermophilic archaeon *Archaeoglobus fulgidus*, designated as Af19, was determined by NMR spectroscopy. Af19 contains three β-strands, two α-helical regions, arranged in a βαββα topology, a 3_{10} helix, and a disordered C-terminal tail. This fold is similar to the βαββαβ RNP motif present in numerous other RNA-binding proteins, which engage their cognate RNAs using conserved sequence motifs present within β-strands 1 and 3. Mutagenesis studies of human SRP19, however, reveal the major contact sites with SRP RNA reside within loops 1, 3, and 4. These contacts were verified by the crystal structure of human SRP19 complexed to SRP RNA helix 6 reported subsequent to the submission of the manuscript. The crystal structure also reveals that, unlike canonical RNP motifs, SRP19 does not engage specific RNA bases through conserved sequence motifs present within β-strands 1 and 3. Instead, SRP19 uses residues both within and flanking β-strand 1 to stabilize the complex through direct and indirect contacts to the phosphate backbone of the tetraloop, leaving the bases of the tetraloop exposed. This, coupled with the fact that SRP19 appears relatively rigid and undergoes only minor changes in structure upon RNA binding, may underlie the molecular basis by which SRP19 functions to initiate SRP assembly.

Keywords: signal recognition particle; SRP19; *Archaeglobus fulgidus*; protein-RNA; NMR, RNP

Introduction

Signal recognition particle (SRP) binds to the signal sequences of proteins destined for cell membranes as the N terminus of the nascent protein appears on the surface of the ribosome (reviewed by Keenan[1]). Components of the SRP have been identified in all organisms studied to date,[2] emphasizing the important role of SRP-mediated protein targeting. The bacterial SRP is composed of one RNA molecule, SRP RNA, and a single protein, named SRP54 or *Ffh*. The more complex well-characterized SRPs of the higher Eucarya contain five additional proteins, SRP9, SRP14, SRP19, SRP68, and SRP72, and a larger RNA of about 300 nucleotides. The secondary structures of the SRP RNAs of Archaea and Eucarya have been shown to be very similar.[3] Recently, the SRP of the hyperthermophilic archaeon *Archaeoglobus fulgidus* was reconstituted from recombinant components, which contains only two SRP proteins, SRP54 and SRP19, bound to RNA.[4]

Significant effort has been directed towards the molecular characterization of SRP components. So far, the structures of a mouse SRP9/14 heterodimer[5] and the *Alu* domain[6] have been determined by X-ray diffraction. Structures of a dimeric 28-mer corresponding to human SRP RNA helix 6[7] and of *Escherichia coli* SRP RNA helix 8[8,9] have also become available. The crystal structure of a tri-

Abbreviations used: Af19, recombinant protein produced in *E. coli*, whose amino acid sequence corresponds to the 104 residue SRP19 protein of *Archaeoglobus fulgidus*; CSI, chemical shift index; RMSD, root-mean-square deviation; NOE, nuclear Overhauser effect; NOESY, nuclear Overhauser effect spectroscopy; RDC, residual dipolar coupling; ppm, parts-per-million; CPMG, Carr, Purcell, Meiboom, Gill.

E-mail address of the corresponding author: hinck@uthscsa.edu

0022-2836/02/010145–14 $35.00/0

meric form of *Ffh* of *Thermus aquaticus* was solved,[10] and a model has been presented for how signal peptides interact within a narrow hydrophobic groove formed by the M-domain of human SRP54.[11] The potential of an RNA-ridge of helix 8 to interact directly with the signal peptide was suggested by the structure of the core of *E. coli* SRP.[12] Despite advances in the cloning and purification of several SRP19 homologues,[4,13] the high-resolution structure of SRP19 has remained unresolved.

The presence of protein SRP19 in an organism correlates well with the occurrence of SRP RNA helix 6,[2] indicating that SRP19 binds to helix 6. Indeed, systematic site-directed mutagenesis of human SRP components demonstrated that helix 6 was required to interact with protein SRP19.[14] Specifically, RNA binding was suggested to involve a tetranucleotide loop (tetraloop) with the consensus sequence GNAR (N is any nucleotide, and R is a pyrimidine). Changes of the conserved adenosine residue at the third position of the tetraloop abolished the RNA binding activity of SRP19.[15] In keeping with the role of SRP19 in directing the assembly of the large domain of SRP (Figure 1) and promoting the association of SRP54, alterations in the distal part of helix 8 also impaired the binding capacity of SRP19.[16] Although SRP19 was the first SRP protein to be cloned, sequenced, and expressed,[13] until recently, little information on the molecular level has been available to explain the crucial role of SRP19 in assembly and function of the SRP.

Herein, we report the solution structure of SRP19 from the hyperthermophilic archaeon *A. fulgidus* (Af19). Af19 adopts a βαββα structure with a topology similar to the RNP motif present in numerous other RNA-binding proteins, suggesting that Af19 might bind SRP RNA through RNP2 and RNP1 motifs, as in RNPs. Mutagenesis studies of human SRP19[17,18] reveal, however, contacts between loops 1, 3, and 4 of the protein and SRP RNA. These contacts were verified by the crystal structure of human SRP19 complexed to SRP RNA helix 6 reported subsequent to the submission of the manuscript.[19] The complex structure also reveals that, unlike canonical RNP motifs, SRP19 does not engage specific RNA bases through RNP1 or RNP2 motifs. Instead, SRP19 utilizes residues both within and flanking β-strand 1 to stabilize the complex through direct and indirect contacts to the phosphate backbone of the tetraloop, thus leaving the tetraloop bases exposed. The significance of this mode of RNA recognition, along with the fact that SRP19 appears relatively rigid and undergoes only minor changes in structure upon RNA binding, are discussed in light of SRP19's role in SRP assembly and function.

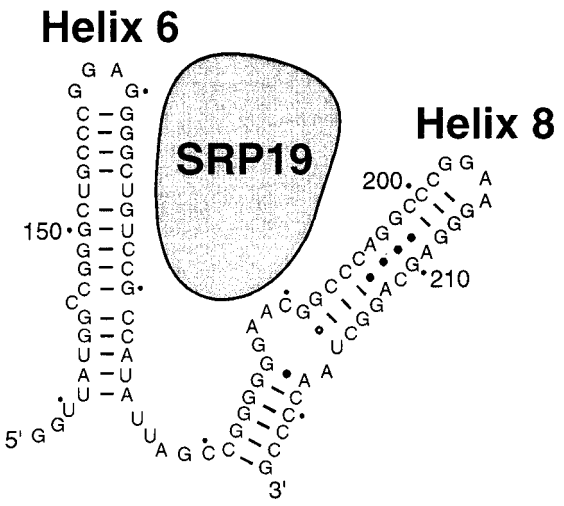

Figure 1. Secondary structure of *A. fulgidus* SRP RNA helices 6 and 8 in relation to protein SRP19. Numbering is according to the full-length molecule in increments of 10, as indicated by the dots and in increments of 50 with numbers. Watson-Crick pairings are shown by lines, a GU pair is connected by a circle, and several non-canonical interactions in helix 8 identified in the structures of homologous components[8,9,12] are shown by large dots.

Results

Assignments

Triple-resonance methodology was used to obtain approximately 90% of the sequential backbone resonance assignments for Af19 at 27 °C and pH 6.0 as reported.[20] All amide ^{1}H-^{15}N correlations, with the exception of M1, Q95, and a nine residue cluster positioned between K53 and E62 were identified in spectra recorded under these sample conditions. Side-chain ^{1}H, ^{13}C, and ^{15}N assignments were approximately 90% complete, although there were a few exceptions involving Lys C^{ε}-H^{ε}, Ile $C^{\gamma 1}$-$H^{\gamma 1}$, and Leu C^{γ}-H^{γ} resonances. No side-chain assignment was made in the K53-E62 region.

Characterization of the unassigned region

Previously, we proposed that the segment between K53 and E62 is a flexible loop whose resonances are broadened by conformational exchange on the millisecond timescale.[20] This conclusion was based upon the observation that there are no unassigned amide protons having significant signal intensity present in either the ^{1}H-^{15}N HSQC or triple-resonance data sets. Further support for the exchange broadening hypothesis followed from the observation that amide protons adjacent to the unassigned segment, such as G63-V66, F48-R49, and E51-K52, exhibit increased signal intensities at 37 °C. Because flexible loop regions within numerous other nucleic acid-bind-

ing proteins have been observed to undergo alterations in their structure and dynamics upon binding their cognate RNA or DNA,[21–24] attempts were made to identify the resonances from the unassigned segment of Af19. The first approach entailed variation in sample temperature and pH so as to shift the loop resonances toward the fast-exchange regime and to decrease the intrinsic amide exchange rates. Experimentally, this was accomplished by recording a series of ^{1}H-^{15}N HSQC spectra in which the temperature, 7-67 °C, and pH, 4.0-7.0, were varied in combination.

These experiments revealed that at pH 6.0, resonances flanking the unassigned loop region exhibit temperature-dependent increases in their signal intensities up to temperatures of approximately 48 °C. Higher temperatures cause no further increase in signal intensity, since the protein begins to unfold. Hence, although heating is effective in shifting the resonances flanking the loop region toward the fast-exchange regime, evidently the effect is too small to enable detection of the loop resonances. Attempts to increase amide signal intensities by lowering the pH were ineffective, since the unfolding transition occurs at significantly lower temperature as the pH is lowered from 6.0 to 4.0.

The second strategy employed involved analysis of a mutant form of Af19 in which the single proline residue within the unassigned region, P56, had been changed to glycine (see Figure 5 for the Af19 amino acid sequence). Because the energetic barrier to proline *cis:trans* isomerization is high,[25] this type of conformational transition typically manifests itself through the appearance of major and minor conformational forms undergoing slow exchange. Thus, any increase in signal intensities caused by the P56G mutation would not be expected to occur through alterations in the rates underlying the exchange, but instead through elimination of conformational heterogeneity within the unassigned region. Consequently, the same type of strategy employed to identify the loop resonances within the wild-type protein was applied to the P56G mutant. Unfortunately, this strategy proved ineffective in enabling the identification of resonances from the unassigned region. Thus, on the one hand it is unclear whether proline *cis:trans* isomerization might contribute to conformational heterogeneity within the unassigned region. On the other, it is evident that the conformational process underlying the broadening within the unassigned loop region does not involve *cis:trans* isomerization about the Y55-P56 peptide bond.

Secondary structure

The secondary structure of Af19 was deduced from the pattern of short-range and medium-range nuclear Overhauser effect (NOE) connectivities and the consensus chemical shift index (CSI),[26] as summarized in Figure 2(a). Together, these data indicate the presence of three β-strands, two α-helical regions, and a single 3_{10} helix. The β-strand regions are supported by weak or medium $d_{\mathrm{N\text{-}N}}(i,i+1)$ and strong $d_{\alpha\text{-}\mathrm{N}}(i,i+1)$ NOE connectivities and a positive consensus CSI. The α-helical regions are supported by strong $d_{\mathrm{N\text{-}N}}(i,i+1)$, weak $d_{\alpha\text{-}\mathrm{N}}(i,i+1)$, and medium-to-weak $d_{\alpha\text{-}\mathrm{N}}(i,i+3)$ NOE connectivities and a negative consensus CSI. The single 3_{10} helical region is supported by the presence of medium $d_{\mathrm{N\text{-}N}}(i,i+1)$ and weak $d_{\alpha\text{-}\mathrm{N}}(i,i+2)$ and $d_{\alpha\text{-}\mathrm{N}}(i,i+3)$ connectivities. The pairing of the three β-strands in an antiparallel fashion is supported by H^{α}-H^{α}, H^{N}-H^{α}, and H^{N}-H^{N} long-range NOEs, as depicted in Figure 2(b). In addition to the secondary structural elements described above, two short β-strands are predicted by the consensus CSI: N10-D12 and K15-S16. These regions are not, however, supported by the short-range NOE data, nor are any long-range NOE connectivities identified that might establish the pairing of these strands with each other, or β-strands 1, 2, or 3. Together, these observations indicate that these regions are extended, but that they do not participate in the formation of a parallel or antiparallel β-sheet.

Solution structure of Af19

The three-dimensional solution structure for Af19 was calculated using the distance geometry-simulated annealing protocol as implemented in a modified form of X-PLOR.[27,28] Initially, the structures were calculated using NOE and dihedral angle restraints alone. The input data consisted of a total of 690 inter-residual NOE distance and 130 dihedral angle restraints (Table 1, left column). Once the overall fold for the protein had been established, another set of structures was calculated whereby 66 one-bond backbone ^{1}H-^{15}N residual dipolar coupling ($^{1}D_{\mathrm{NH}}$ RDC) restraints were included in the final stage of refinement (Table 1, right column). The latter calculations served to validate the structures calculated from the NOE and dihedral restraints alone, as evidenced by the quality factor, Q, describing the agreement of the $^{1}D_{\mathrm{NH}}$ RDC data with the calculated structures, which decreased from a value of 0.77 ± 0.02 prior to RDC refinement to 0.31 ± 0.03 following RDC refinement (Table 1). Overall, the structures calculated with and without RDC restraints were found to be highly similar to one another, having a mean pairwise RMSD in backbone atom positions of 1.05 Å, and differing only slightly with respect to their calculated precision (see below).

The ensemble of calculated structures consistent with the experimental NOE, dihedral, and RDC restraints (26/47) is shown in Figure 3(a). Both this ensemble, and the ensemble of structures calculated without RDC restraints, showed excellent precision among the ordered regions, 0.6-0.9 Å (see below), good covalent geometry, and low overall energies. For each ensemble, close to 90 % of the residues lie in the most favored region of the Ramachandran plot. A summary of the statistics

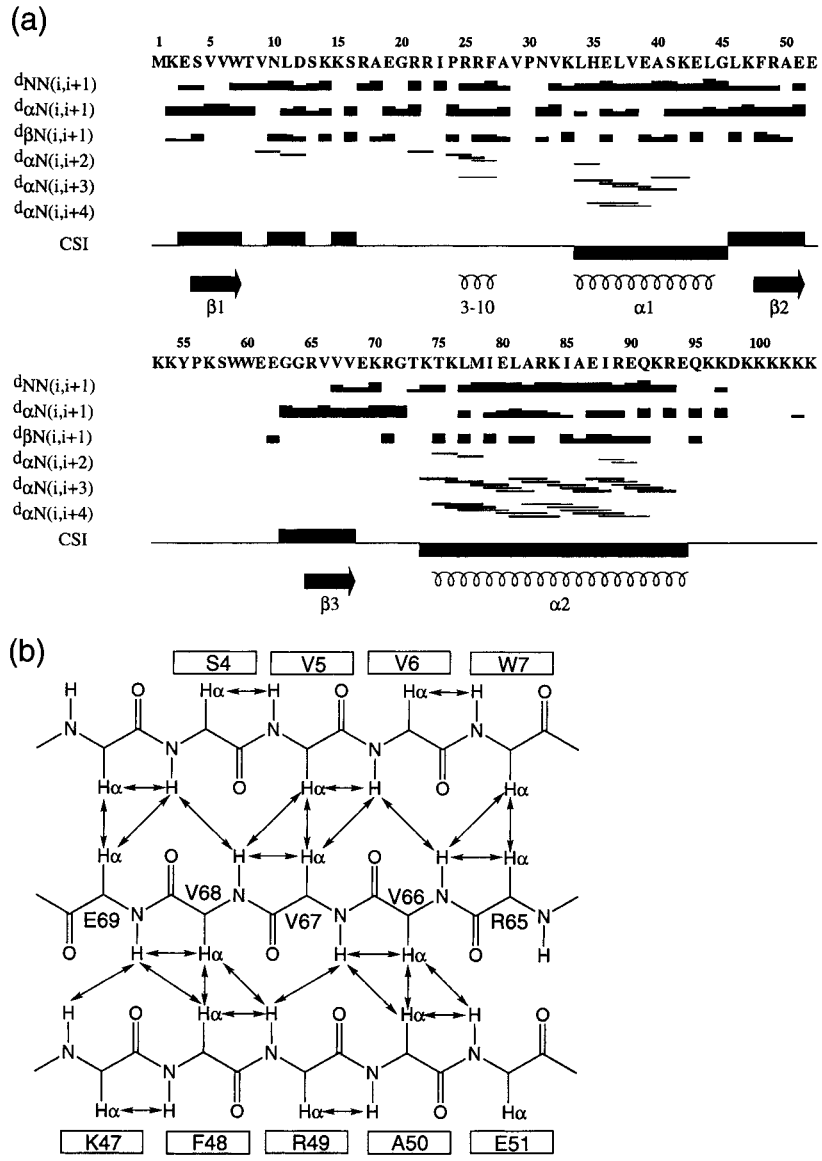

Figure 2. Secondary structure of Af19. (a) Secondary structure as deduced from sequential and short-range NOE connectivities and the chemical shift index (CSI)[26]. Sequential NOE connectivities , $d_{N\text{-}N(i,i+1)}$, $d_{\alpha\text{-}N(i,i+1)}$, $d_{\beta\text{-}N(i,i+1)}$, are classified according to relative distance with increasing bar height corresponding to decreasing distance. Short-range NOE connectivities are indicated by horizontal bars that link the first and second residues involved in the cross-peak. CSI C^{α}, C^{β}, C^{O}, and H^{α} consensus values are shown, upward boxes corresponding to β-conformation, downward boxes corresponding to α-conformation, and other regions corresponding to coil. The secondary structure of Af19, as deduced using the criteria established by Kabsch & Sander,[48] is diagrammed on the lower part of the Figure. (b) An illustration of the triple-stranded antiparallel β-sheet of Af19. Double-ended arrows indicate sequential and long-range NOE connectivities that have been identified.

describing both ensembles is provided in Table 1. A ribbon diagram depicting the energy-minimized average NOE, dihedral, and RDC structure is shown in Figure 3(b). The overall fold consists of two α-helices, arranged roughly perpendicular to one another, and packed against one face of a triple-stranded antiparallel β-sheet. The fold is compact, with α-helix 2 lying in a groove formed by α-helix 1 and loop 1, a 26-residue segment bridging the C-terminal end of β-strand 1 with the N-terminal end of α-helix 1.

Disorder *versus* flexibility

A superposition of the ensemble of structures calculated on the basis of the experimental data relative to the mean reveals that the majority of the protein backbone is well determined. There are, however, a few exceptions to this generalization. Residues K53-E62 in loop 3 and residues 95-104 in the C-terminal tail exhibit considerable disorder over the ensemble of calculated structures (Figure 4(a)). In addition, there are slight increases in disorder over the three assigned loop regions, L1, L2, and L4. In each case, the apparent disorder correlates inversely with the restraint density, as illustrated in Figure 4(a)(b). The RMSDs in the coordinates when these and various other amino acid segments are omitted in the alignment are summarized in Table 2. The ensemble of structures calculated based on NOE, dihedral, and RDC restraints exhibits a backbone RMSD of 0.62 Å and 0.26 Å, respectively, when the ordered parts of the protein (K2-E52, G63-Q95) and the regular elements of secondary structure are considered (Table 2B). RMSDs for the ensemble of structures calculated based on NOE and dihedral restraints alone are higher, on average, by 0.05-0.2 Å (Table 2A), presumably because of the smaller number of restraints used in the calculation.

Table 1. Distance, dihedral, and residual dipolar coupling restraints statistics for the structure of Af19

	Structures calculated using NOE and dihedral restraints		Structures calculated using NOE, dihedral, and RDC restraints	
A. *Restraint summary*				
Total	820		886	
NOE distance restraints	690		690	
Intraresidue ($i-j=0$)	0		0	
Sequential ($\|i-j\|=1$)	195		195	
Short range ($1<\|i-j\|=5$)	237		237	
Long range ($\|i-j\|>5$)	258		258	
Dihedral restraints	130		130	
ϕ	65		65	
ψ	65		65	
$^1H/^{15}N$ RDC restraints	0		66	
Accepted structures[a]	42/50		26/47	
B. *RMSD from idealized covalent geometry and experimental restraints*				
	$\langle Af19\rangle_r$[b]	{Af19}[b]	$\langle Af19\rangle_r$[b]	{Af19}[b]
Bonds (Å)	0.003	0.0022 ± 0.0001	0.003	0.0027 ± 0.0001
Angles (deg.)	0.57	0.57 ± 0.01	0.69	0.67 ± 0.02
Impropers (deg.)	0.47	0.45 ± 0.02	0.66	0.68 ± 0.02
NOE distance restraints (Å)	0.045	0.044 ± 0.004	0.066	0.056 ± 0.005
Dihedral angle restraints (deg.)	0.72	0.88 ± 0.14	1.89	2.13 ± 0.11
$^1D_{NH}$ RDC restraints (Hz)			1.48	1.11 ± 0.10
$^1D_{NH}$ quality factor[c]	0.77	0.77 ± 0.02	0.45	0.31 ± 0.03
F_{NOE} (kcal/mol)[d]	42.9	41.7 ± 7.6	93.8	67.3 ± 1.1
$F_{Dihedral}$ (kcal/mol)[e]	4.1	6.3 ± 2.2	28.5	36.1 ± 3.6
F_{RDC} (kcal/mol)[f]			355	182.1 ± 11.1
C. *Ramachandran statistics*[g]				
Residues in most favored region (%)	90.9		88.4	
Residues in additional allowed regions (%)	4.1		6.7	
Residue in generously allowed regions (%)	4.1		3.6	
Residues in disallowed regions (%)	0.9		1.3	

[a] Acceptance criteria: NOE distance violations <0.5 Å, dihedral angle violations <30°, and residual dipolar coupling violations <3.0 Hz.
[b] {Af19} is the ensemble of accepted structures; $\langle Af19\rangle_r$ is obtained by restrained minimization of the average of {Af19}.
[c] Defined according to Cornilescu.[38]
[d] Calculated using a soft-square-well potential, sum averaging, a scale factor of 30, a square-well constant of 1.0, and ceiling of 100 kcal/mol.[27]
[e] Calculated using a square-well potential and a scale factor of 10.[27]
[f] Calculated using a harmonic potential and a force constant of 2.5.[27]
[g] The Ramachandran statistics are calculated over the ensemble of accepted structures and include only the ordered regions of the protein, residues 3-52 and 63-94. The statistics themselves were calculated using the program PROCHECK-NMR.[52]

Measurements of backbone ^{15}N longitudinal (T_1) and transverse (T_2) relaxation times and ^1H-^{15}N NOE steady-state NOE values for Af19, as shown in Figure 4(c)-(e), reveal that with the exception of residues Q95-K104 in the C-terminal tail, the relaxation parameters are relatively uniform over the length of the protein backbone. Thus, the disorder of the C-terminal segment evident among the ensemble of calculated structures correlates well with internal flexibility in solution on the nano- to picosecond timescale, as judged by ^{15}N relaxation data measurements (Figure 4(c)-(e). The slight increase in disorder observed among the three assigned loop regions, L1, L2, and L4, on the other hand correlate poorly with internal flexibility in solution, as judged by the lack of significant deviation of the ^{15}N relaxation data measurements away from their average values. Thus, the elevated disorder apparent among the ensemble of calculated structures in the L1, L2, and L4 loop regions appears to be a consequence of the lower than average restraint densities in these regions and not enhanced flexibility on the nano- to picosecond timescale.

The disorder of residues within loop 3 evident among the ensemble of calculated structures is entirely due to the lack of experimental restraints for this part of the chain. Therefore, no conclusion can be drawn regarding internal flexibility within this region of the protein based upon the apparent structural disorder. As discussed earlier, resonances within this loop region appear to undergo exchange broadening owing to (a) conformational transition(s) occurring on the millisecond timescale. As shown, the conformational transition underlying the observed broadening does not appear to be *cis:trans* isomerization of the Y55-P56 peptide bond. These results, and independent mutagenesis studies which indicate that P56 and K57 within loop 3 contact SRP RNA (see below),[17,18] suggest that the conformation of the K53-E62 loop region is determined, in part, by its contact with SRP RNA. Hence, it is possible that loop 3 undergoes conformational rearrangements between RNA-bound

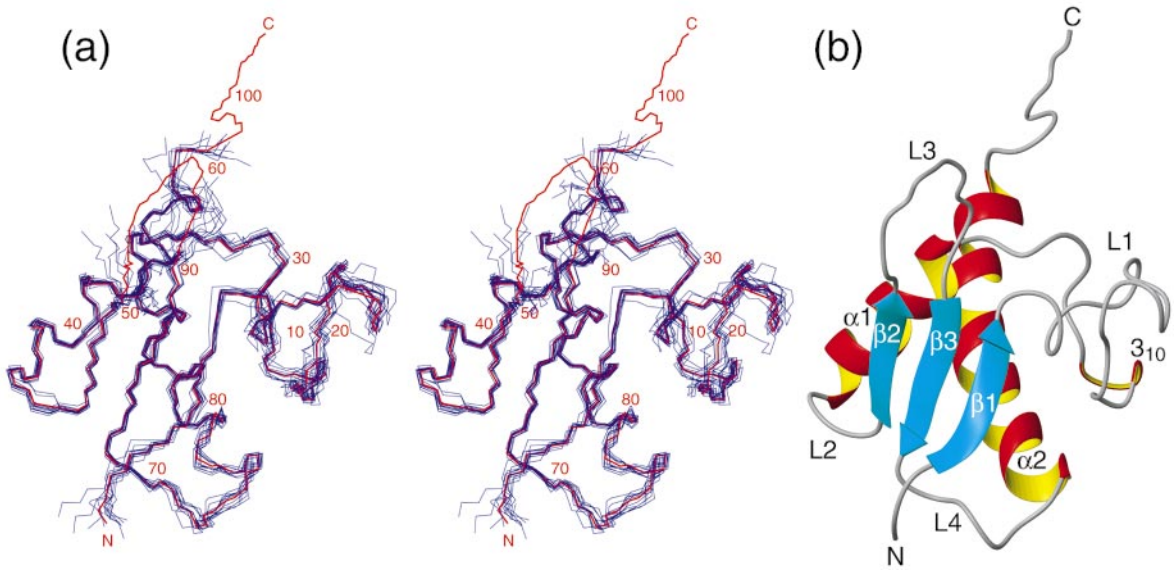

Figure 3. NMR solution structures of Af19. (a) A stereoview of the ensemble of the ten lowest-energy structures (blue) superimposed on the basis of the deduced secondary structure[48], residues β1 4-7, 3_{10} 25-27, α1 34-44, β2 48-51, β3 65-68, α2 75-94. The mean structure is depicted in red. Only backbone heavy atoms are shown. Residues 53-60 and 98-104 are highly disordered among the ensemble of accepted structures. For the purposes of clarity, these two regions are not displayed among the ensemble of ten lowest-energy structures. (b) A MOLMOL[49] ribbon diagram of the energy-minimized average Af19 structure in which the regular elements of secondary structure are identified.

and free conformations, or other low-energy conformations unrelated to RNA binding.

Discussion

The structure of Af19 reveals a compact structure having a mixed α/β architecture and a βαββα topology (Figure 3(b)). This fold exhibits strong resemblance to the RNP domain, characterized by a βαββαβ fold, present in numerous other RNA-binding proteins, most notably the single-stranded RNA binding protein U1A[30] as depicted in Figure 5(a). RNP domains recognize their cognate RNAs using conserved motifs, designated as RNP1 and RNP2, present in the first and third β-strands, respectively.[31] These motifs are comprised of polar, non-polar, and aromatic amino acid residues that interact with exposed bases of the RNA to enable the recognition of specific RNA sequences. This is depicted schematically in Figure 5(a) for the complex of U1A bound to a 21 nt RNA hairpin[30] where the bases of the RNA that interact with the RNP1 and RNP2 motifs are colored green and magenta, respectively. The βαββα RNP-like domain present in Af19 also appears in the anticodon-binding domain of phenylalanine tRNA synthetase (Figure 5(b)). The crystal structure of this enzyme complexed to $tRNA^{Phe}$ reveals the first and last two bases of the anticodon are recognized by amino acid residues that reside within RNP1 and RNP2-like motifs, respectively (Figure 5(b)).[32] Thus, the striking structural similarity of the βαββα anticodon binding of phenylalanine tRNA synthetase and canonical RNP domains, such as U1A is not coincidental.

Table 2. Coordinate RMSD of Af19

Structures[a]	All		Ordered		Secondary	
	bb[b]	Heavy	bb	Heavy	bb	Heavy
A. *Structures calculated using NOE and dihedral restraints*						
{Af19} *versus* ⟨Af19⟩	2.10	3.07	0.87	1.46	0.36	1.25
⟨Af19⟩ *versus* $\langle Af19\rangle_r$	1.09	1.85	0.52	0.79	0.23	0.72
B. *Structures calculated using NOE, dihedral, and RDC restraints*						
{Af19} *versus* ⟨Af19⟩	2.04	2.97	0.62	1.41	0.26	1.21
⟨Af19⟩ *versus* $\langle Af19\rangle_r$	1.01	1.67	0.51	0.81	0.46	0.77

[a] {Af19} is the ensemble of accepted structures; ⟨Af19⟩ is the mean of {Af19}; $\langle Af19\rangle_r$ is obtained by restrained minimization of ⟨Af19⟩. Reported RMSD values are in units of Å.

[b] bb includes the backbone atoms, N^H, C^α, and C^O; Heavy includes all non-hydrogen atoms; All includes residues 1-104; Ordered includes 3-52 and 63-94; and Secondary includes residues 4-7, 25-27, 34-44, 48-51, 65-68, and 75-94.

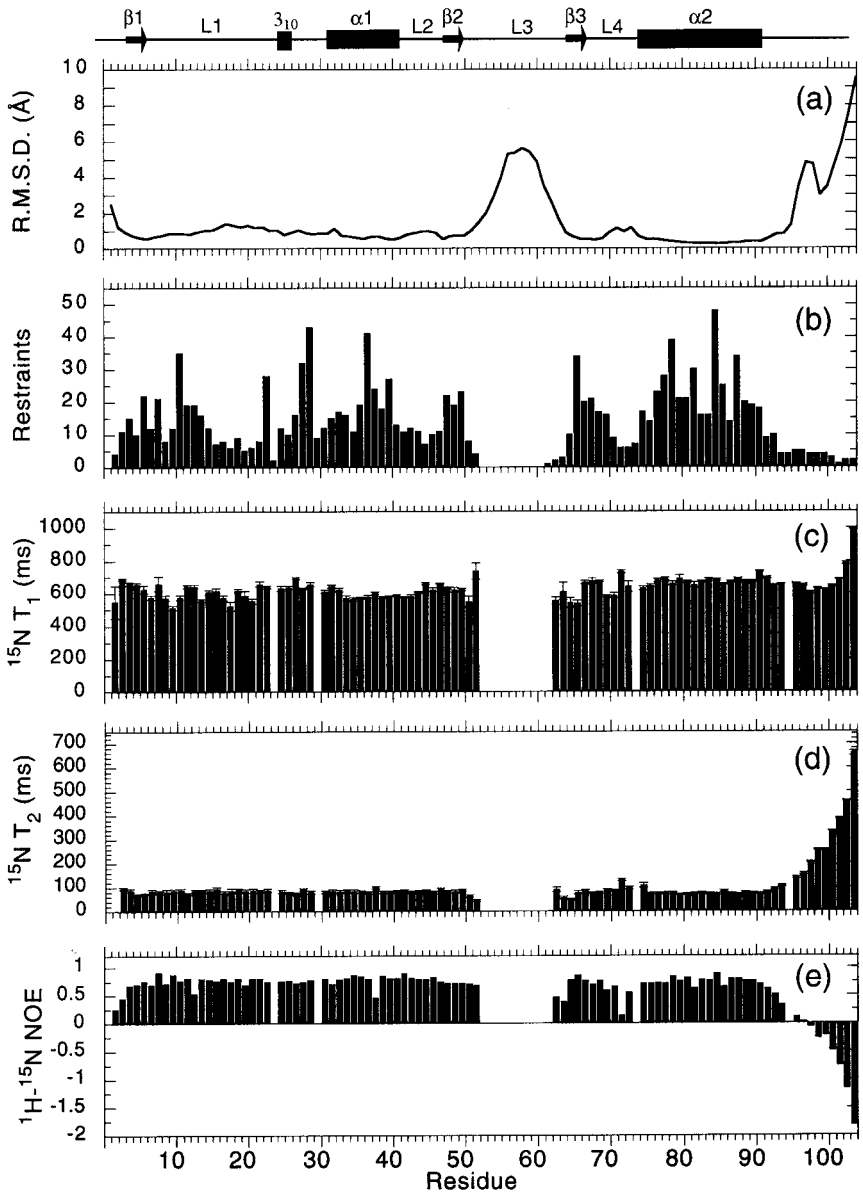

Figure 4. Disorder and flexibility of Af19. (a) Residue RMSDs for the ensemble of 26 accepted structures *versus* the mean structure. (b) The number of inter-residual NOE distance restraints on a per-residue basis. (c) Backbone ^{15}N transverse (T_1) relaxation times for Af19 at 27° C and pH 6.0. The data were acquired at an ^{15}N frequency of 50.68 MHz using a ^{15}N 90° pulse-width of 40 μs. (d) Backbone ^{15}N transverse (T_2) relaxation times for Af19 measured using a CPMG sequence with a spacing of 500 μs between 180° pulses in the CPMG pulse train. (e) Steady-state backbone ^{1}H-^{15}N NOE values for Af19 determined by recording the signal intensities in two experiments, one with a series of proton presaturation pulses and one with the presaturation period replaced by a delay of equal length (2.9 seconds). All other acquisition parameters are identical with those of the T_1 measurements. The protein secondary structural elements are indicated at the top of the Figure.

To explore whether Af19 might recognize SRP RNA through mechanisms used by RNPs, such as U1A, or related domains, such as the anticodon-binding domain of phenylalanine tRNA synthetase, the results from two complementary mutagenesis studies of human SRP19 were considered.[17,18] The first involved the systematic replacement of pairs of amino acid residues with glycine throughout the length of human SRP19, representing a total of 53 unique mutants.[17] The second involved the directed replacement of 13 conserved basic amino acid residues with glutamine.[18] A summary of the results of these studies is presented along the lower part of the SRP19 sequence alignments shown in Figure 6, and a visual representation of these data is presented in Figure 7(a)(b), where mutations within human SRP19 that abolish binding to full-length SRP RNA are mapped onto the structure of Af19.

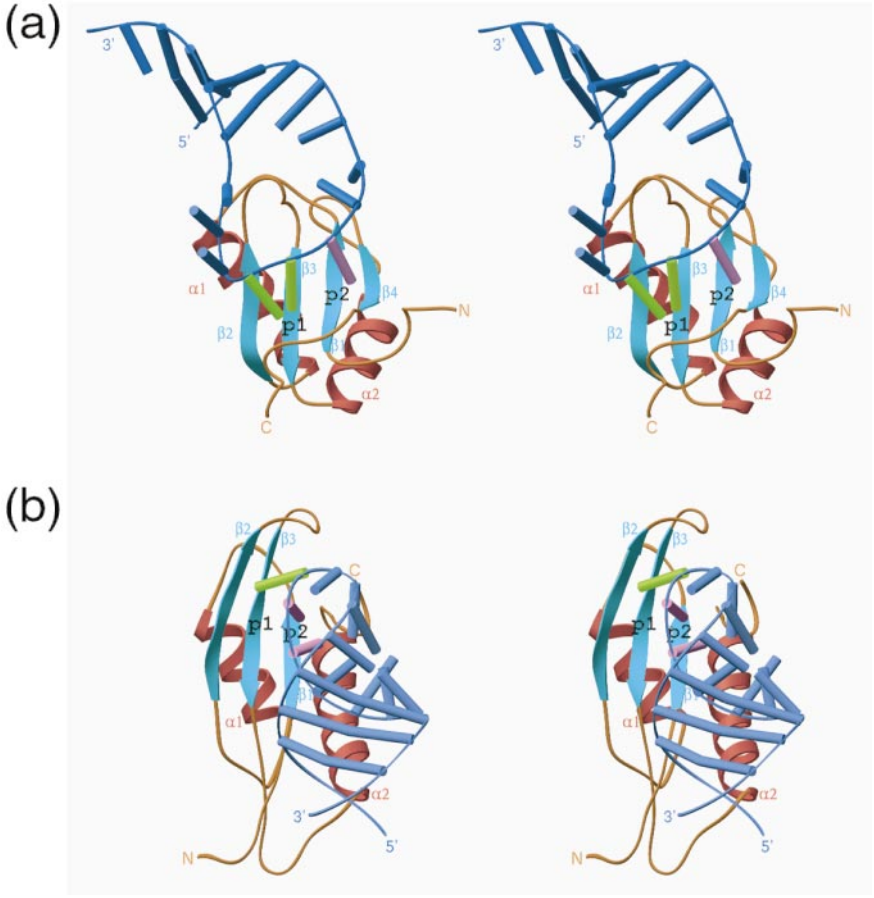

Figure 5. RNA-binding proteins exhibiting the RNP motif and their mode of interaction with their cognate RNAs. (a) A stereo diagram of the single-stranded RNA-binding protein U1A complexed with a stem loop RNA fragment with a 5′ AUUGCAC 3′ loop sequence (PDB code 1URN).[30] The backbone of the RNA fragment and the bases are depicted schematically in dark blue. The first and last two bases of the loop trinucleotide, C10-A11-C12, which interact with the RNP2 and RNP1 sites are shown in magenta and green, respectively. The RNP1 and RNP2 sites are designated as p1 and p2, respectively. The protein secondary structure and the protein and RNA chain termini are labeled. (b) A stereo diagram of the anticodon-binding domain of *Thermus thermophilus* phenylalanine-tRNA synthetase complexed with $tRNA^{Phe}$ (PDB code 1EIY).[32] The portion of the structure shown corresponds to residues 687-785 of the B domain of phenylalanine-tRNA synthetase and nucleotides 23-45 corresponding to the anticodon loop of $tRNA^{Phe}$. The backbone of the RNA fragment and the bases are depicted in dark blue. The first and last two bases of the anticodon, G34-A35-A36, which interact with the RNP1 and RNP2 sites are shown in green and magenta, respectively. The RNP1 and RNP2 sites are designated as p1 and p2, respectively. The protein secondary structure and the protein and RNA chain termini are labeled. (a) and (b) were generated with the program RIBBONS.[50]

As shown in Figure 7(b), contact sites exist throughout the SRP19 secondary structure, including putative RNP2- and RNP-like motifs present within β-strands 1 and 3, raising the possibility that SRP19 engages SRP RNA through motifs analogous to those used by RNPs. However, since glycine substitutions at adjacent positions are anticipated to be destabilizing in the regions of regular secondary structure, the degree of confidence to which such contacts can be identified is relatively low. Other contacts that can be identified with a higher degree of confidence include residues within loop regions 1 (K15, R21, and R22), 3 (K57), and 4 (K74), where the effects of the mutations on stability would be expected to be minimal and where consistent negative results are obtained with both the diglycine and glutamine mutants (Figure 6). As shown in the leftmost panel of Figure 7(c), loop regions 1, 3, and 4 of Af19 contain the majority of basic amino acid residues, and it appears reasonable that this face of the molecule is in direct contact with SRP RNA.

Despite the intimate involvement of SRP19 in binding to two RNA helices, it is interesting to note that the opposite face, Figure 7(c), rightmost panel, lacks basic residues as well as mutations found to affect RNA binding. Consequently, this face is less likely to be in contact with RNA. Consistent with previous results,[33] the lysine-rich C-terminal tail that does not play a role in RNA binding, extends from the folded structure and is structurally disordered. Thus, SRP19 and the anticodon binding domain of phenylalanine tRNA synthetase are similar, in that the principal site of

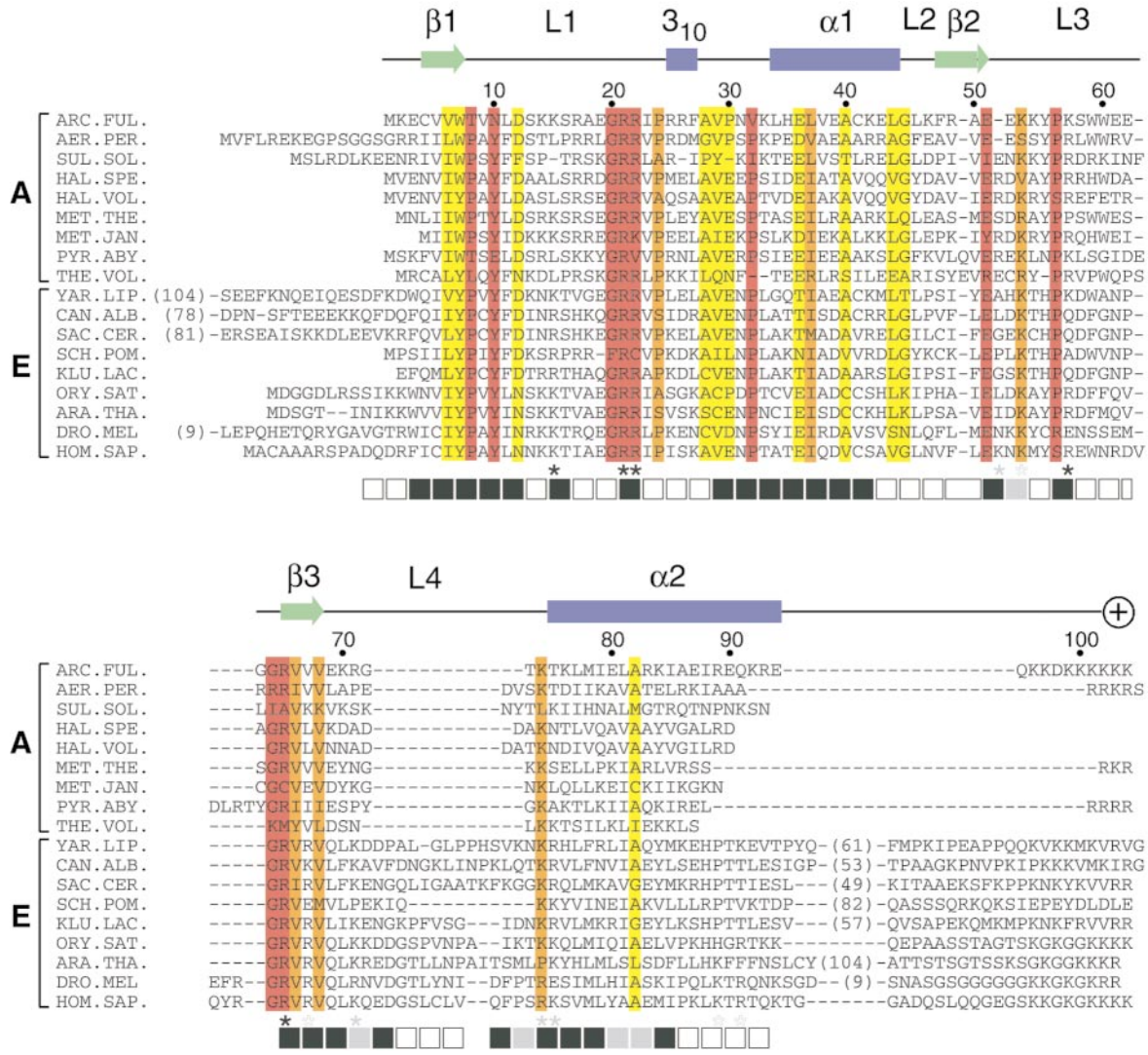

Figure 6. Alignment of representative SRP19 sequences. Marked are the α-helices (α1 and α2), the 3_{10} helix, β-strands (β1-β3), loops 1 to 4 (L1-L4), and the positively charged C-terminal tail. The Af19 sequence is shown on top of each panel with residues numbered in ten residue increments. Species are grouped as Archaea (A) and Eucarya (E) with their names abbreviated as in the SRPDB[2]. Bracketed numbers near the termini indicate the number of inserted residues present in some species. Dashes indicate alignment gaps. Highly conserved residues are shown on a red background; residues of intermediate and lower conservation are highlighted in orange and yellow, respectively. Asterisks directly below the human SRP19 sequence indicate lysine to glutamine or arginine to glutamine amino acid substitutions introduced into human SRP19 that either completely (black) or partially (gray) abolished binding to full-length SRP RNA. Open asterisks designate those residues which when mutated had no detectable effect upon SRP RNA binding.[18] Squares below the human SRP19 sequence indicate diglycine substitutions that abolish binding to full-length SRP RNA completely (black) or partially (gray). Open squares designate pairs of residues that, when mutated, had no detectable effect upon SRP RNA binding.[17]

RNA interaction appears to occur through the β1-edge of the central triple-stranded sheet. It is unclear, however, from this analysis whether SRP19 might use RNP1-like or RNP2-like motifs to engage SRP RNA, since it is possible that mutants identified in such regions of SRP19 are structurally disruptive.

Subsequent to the submission of the manuscript, the crystal structure of a C-terminal truncated form of human SRP19 complexed to a 29 nt RNA fragment corresponding to SRP RNA helix 6 was reported.[19] The structures of Af19 and the RNA-bound form of human SRP19 agree well, having backbone RMSDs of 2.2 Å and 2.3 Å for the structures calculated with and without RDC restraints, respectively. Not included in this comparison are loops 3 and 4. Loop 3 contacts the RNA in the complex as anticipated, and loop 4 is lengthened by 11 residues in human SRP19.

As discussed above, SRP19 appears to interact with SRP RNA using structural features similar to those used by the anticodon-binding domain of phenylalanine tRNA synthetase.[32] However, the crystal structure of the human SRP19-helix 6 com-

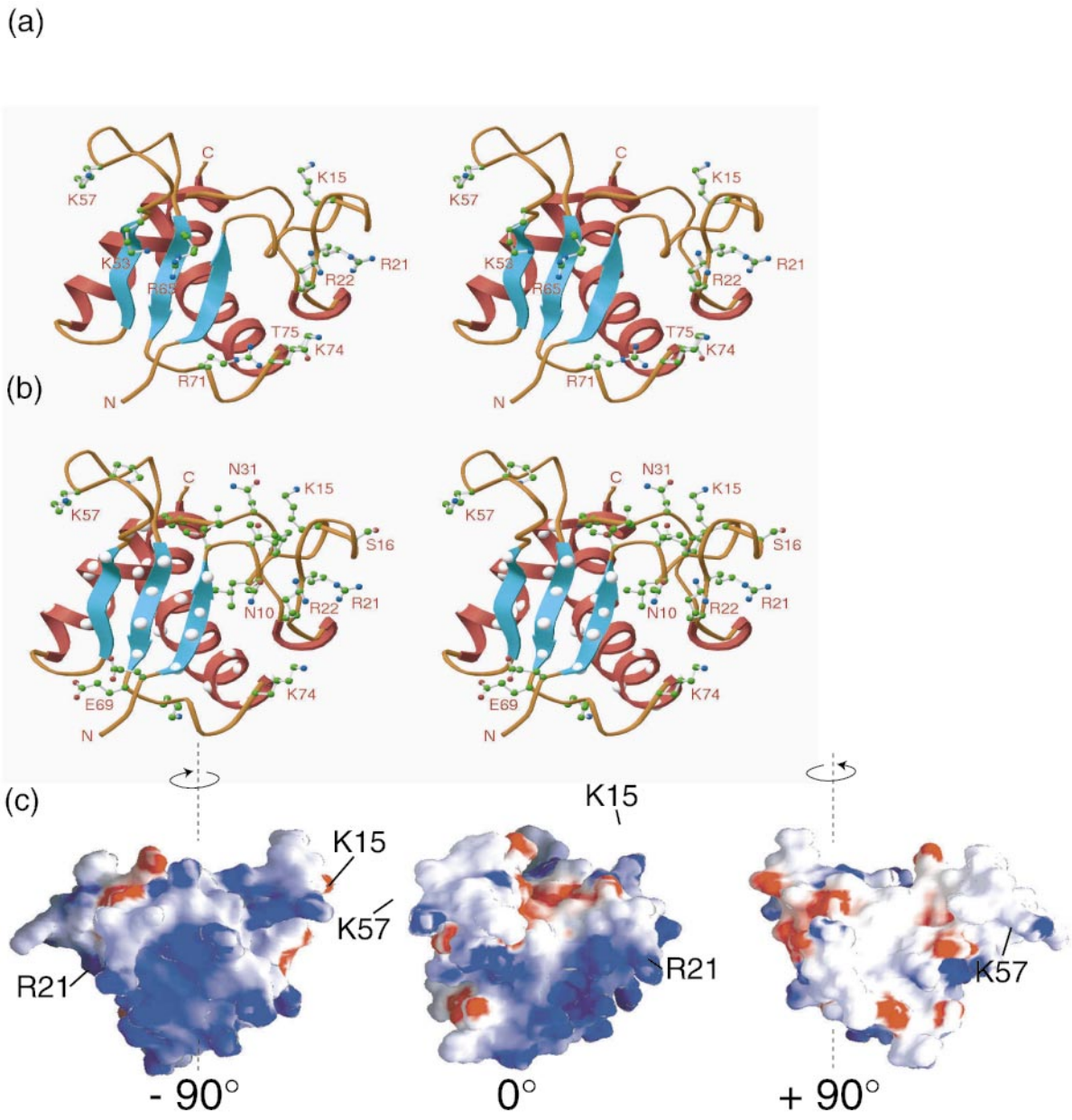

Figure 7. Af19 RNA-binding regions. (a) A stereo ribbon diagram of Af19 showing the conserved basic residues (ball-and-stick showing the full amino acid side-chain) that, upon mutation, to glutamine abolish binding to SRP RNA in human SRP19.[18] (b) A stereo ribbon diagram of Af19 depicting diglycine mutations that abolish binding to SRP RNA in human SRP19.[18] The affected residues in loop regions are shown as ball-and-stick representations of the full amino acid side-chain. Affected residues in regular secondary structures are depicted by a single white sphere at the position of the C^{α} carbon atom for that amino acid. (a) and (b) were generated with the program RIBBONS.[50] (c) Surface representations of Af19 generated by the program GRASP.[51] Basic residues are labeled in blue and acidic residues in red. The zero degree (0°) view of the molecule is oriented as shown above in (a) and (b), or rotated, as indicated below each representation. The C-terminal tail, residues 95-104, has been omitted from (a)-(c).

plex reveals that the orientations of the RNA relative to the protein differ. In phenylalanine tRNA synthetase, the anticodon loop is near the C-terminal end of β-strand 1, the minor groove of the proximal loop segment is filled by amino acid residues that extend from the C-terminal segment of the protein, and the distal end of the RNA lies closest to the N-terminal end of β-strand 1. Recognition of the first and second two bases of the anticodon occurs through residues that comprise RNP1-like and RNP2-like motifs within β-strands 1 and 3, respectively (Figure 5(b)). In SRP19, the RNA assumes the reverse orientation, whereby the tetraloop segment of the RNA lies near the center of β-strand 1 and the proximal stem of the RNA lies adjacent to loop 1 at the C-terminal end of β-strand 1. The interactions that stabilize the complex include loops 1 and 3, which fill the major

groove of the stem, and residues flanking and within β-strand 1, which contact the backbone atoms of the helix 6 tetraloop. Importantly, this mode of interaction leaves the bases of the tetraloop exposed, possibly to interact with helix 8 as proposed.[19] Hence, the anticodon-binding domain of phenylalanine tRNA synthetase and SRP19 appear to have adapted their RNP-like βαββα scaffold to recognize their cognate RNAs in different ways in order to satisfy their diverse functional roles.

The description of free Af19 complements the description of the human SRP19-helix 6 complex by providing information regarding the extent to which the protein structure adapts to accommodate the RNA. The remarkable similarity of the overall conformation of free Af19 and the human RNA-bound SRP19 indicates that only minor changes in the structure of SRP19 occur upon RNA binding. Of interest is loop 1, which exhibits extensive contacts with the RNA, as indicated by a contact area of 281 Å^2. The backbone conformation of loop 1 of human SRP19 has an RMSD of 1.1 Å relative to the same region in Af19, indicating that SRP19 is capable of adopting the RNA-bound conformation even in the absence of its cognate RNA. Evidently, SRP19 is relatively rigid, which may be important for fulfilling its role as the initiator of SRP assembly and for inducing changes in the conformation of the SRP RNA as suggested.[34] Since the structure of free human SRP19 is unknown, we cannot exclude the possibility that the proposed binding mechanism is relevant only to Af19 and possibly other thermophilic archaea.

The idea that SRP RNA simply adjusts to accommodate the binding of Af19 requires modification with respect to other regions of the protein. Loop 3 evidently reorders and adopts a single conformation with direct-protein RNA contact upon associating with RNA. Thus, the association between SRP19 and SRP RNA helix 6 appears to occur through mutual accommodation of both the protein and RNA surfaces, as has been observed in numerous other protein-RNA complexes (reviewed by Draper[35]). The significance of this mechanism in the context of SRP assembly is that the conformation of the RNA induced by SRP19 binding may be important for initiating the binding of other SRP proteins, such as SRP54.

Materials and Methods

Sample preparation

The 104 residue recombinant *A. fulgidus* SRP19 protein containing cysteine to serine substitutions at positions 4 and 41, designated Af19, was expressed and purified as described.[20] The substitutions at positions 4 and 41 served to prevent covalent dimer formation over the extended periods required for NMR data collection, but did not affect binding to *A. fulgidus* SRP RNA *in vitro* (C.Z., unpublished observation). Samples for NMR spectroscopy were prepared by exchanging ^{15}N or ^{15}N/^{13}C uniformly labeled Af19 protein into buffer containing 25 mM KH_2PO_4, 50 mM NaCl and 5 % or 99.99 % ^2H_2O at pH 6.0. Samples were approximately 280 μl in volume and were contained in a 5 mm thin-wall NMR micro cell (Shigemi, Allison Park, PA). Protein concentrations were between 1.8 and 2.2 mM as judged on the basis of the calculated extinction coefficient, 1.00 $A_{280} = 0.69$ mg/ml.

Site-directed mutagenesis

The P56G variant of Af19, which contained a proline to glycine substitution at position 56, was prepared by mutating the gene encoding Af19 in the expression vector pET23d using a PCR-based strategy.[36] P56G Af19 was isotopically labeled, purified, and prepared for NMR spectroscopy using the procedure outlined above.

NMR spectroscopy

NMR spectra were acquired at a field strength of 11.7 T using a three-channel Bruker AMX2-500 spectrometer equipped with a ^{1}H/^{13}C/^{15}N triple-resonance 5 mm probe fitted with a single-axis (*z*) pulsed-field gradient coil. All NMR spectra were collected at a sample temperature of 27° C, except for the residual dipolar coupling data, which were collected at 37 °C (see below). Backbone and aliphatic side-chain ^{1}H, ^{13}C, and ^{15}N sequential resonance assignments for Af19 were made using triple-resonance methods as reported.[20] Additional assignments for histidine and tyrosine $H^{\varepsilon,\delta}$ and $C^{\varepsilon,\delta}$ resonances and phenylalanine $H^{\varepsilon,\delta,\zeta}$ and $C^{\varepsilon,\delta,\zeta}$ resonances were made by first identifying H^{β}-H^{δ} NOEs in the 3D ^{13}C-edited NOESY spectrum (see below). The aromatic spin systems were then assigned using a high-resolution 2D NOESY spectrum and a natural abundance ^{1}H-^{13}C HSQC spectrum optimized for the aromatic region.

Distance restraints were derived primarily from 3D ^{15}N and ^{13}C-edited NOESY data sets using mixing times (τ_m) of 120 ms. Ambiguities that arose in the assignment of NOEs in these data sets were further resolved using a 4D ^{13}C, ^{13}C-edited NOESY spectrum ($\tau_m = 90$ ms) and a 3D ^{15}N-edited NOESY spectrum with ^{13}C chemical shift evolution in the F_2 dimension ($\tau_m = 134$ ms), respectively. Distance restraints for structure calculations were derived by interactively analyzing the four NOE data sets using the program PIPP.[37] The initial set of NOE crosspeaks were limited to those defining the secondary structure of the protein, along with several unambiguous NOEs involving residues that pack in the hydrophobic core. In successive iterations, NOEs were added to the restraint tables provided either the symmetry-related crosspeak was present in the ^{13}C-edited NOE data set, as in the case of aliphatic-aliphatic NOEs, or the observed NOE crosspeak was present in both the ^{15}N-edited and ^{15}N-edited/^{13}C-edited NOE data sets, as in the case of amide-aliphatic NOEs.

Backbone torsion angle restraints for φ and ψ were derived from analysis of $^1H^{\alpha}$, $^{13}C^{\alpha}$, $^{13}C^{\beta}$, $^{13}C^{O}$, and ^{15}N chemical shifts as implemented in the program TALOS.[38] TALOS dihedral restraints were applied to all residues for which a statistically significant fit was obtained and were assigned an error range of ±30°.

One-bond ^{1}H-^{15}N residual dipolar coupling (RDC) restraints for Af19 were obtained by measuring the apparent ^{1}H-^{15}N one-bond *J*-couplings, $^1J_{NHapp}$, for a sample of the protein in either an unstressed or mechanically stressed 8.0 % (w/v) polyacrylamide (acrylamide/bisacrylamide, 29:1, w/w) gel. The gel sample was prepared using the dehydration/rehydration procedure as

described.[39] The fully hydrated gel cylinder had a length of 21.0 mm and a diameter of 3.6 mm. The extent of the vertical compression for the mechanically stressed sample was approximately 19 %, corresponding to a final length of 17.0 mm and a final diameter of 4.1 mm. Values for $^1J_{NHapp}$ were measured using the IPAP-HSQC method[40] at a sample temperature of 37 °C. The higher temperature was found to be necessary to compensate for the decrease in rotational correlation that accompanied incorporation of Af19 into the gel matrix. The ^{1}H-^{15}N HSQC spectrum obtained under these conditions was virtually identical with that obtained for Af19 in isotropic solution at 27 °C, indicating that the altered sample conditions had no significant effect on the structure of the protein and justifying the use of the measured RDCs in combination with the NOE and dihedral angle restraints determined at the lower temperature to calculate the structure. The one-bond ^{1}H-^{15}N residual dipolar couplings, $^1D_{NH}$, were calculated by subtracting $^1J_{NHapp}$ measured in the presence of mechanical stress, $^1J_{NHapp} = {}^1J_{NH} + {}^1D_{NH}$, from those measured in the absence of stress, $^1J_{NHapp} = {}^1J_{NH}$.

Structure calculations

Structure calculations were carried out with the distance geometry/simulated annealing protocol[41] using a modified form of X-PLOR 3.851.[27,28] NOE cross-peak intensities were converted into distances by first normalizing each to the intensity of the corresponding diagonal peak, and by using a modified form of the isolated two-spin approximation[42,43] to calculate distances. The calculated distances, along with a 1.8 Å lower distance bound and appropriate pseudo-atom corrections for methylene, methyl, and non-stereospecifically assigned methyl groups of leucine and valine residues, were then used as input for structure calculations. The $^1D_{NH}$ restraints were implemented using the computational strategy described by Clore.[28] Estimates of the axial component, D_a, and rhombicity, R, of the molecular alignment tensor were obtained from analysis of the measured RDCs using the method of singular value decomposition as implemented in the program PALES.[44] The RDC data set used for these calculations included $^1D_{NH}$ values for all residues except those exhibiting significant overlap in the 2D HSQC spectrum or those exhibiting significant internal flexibility (^{1}H-^{15}N NOE < 0.6, see below).

Backbone ^{15}N relaxation parameters

Backbone amide nitrogen T_1, T_2, and ^{1}H-^{15}N NOE relaxation parameters were measured using ^{15}N Af19 and the ^{1}H-detected pulse schemes as described.[45] The data sets consisted of multiple interleaved timepoints with variable relaxation delays of 8.0, 96.0, 200.0, 256.0 296.0, 352.0, 400.0, 504.0, 600.0, 800.0, and 1000.0 ms for T_1 and 8.0, 16.0, 24.0, 32.0, 40.0, 48.0, 56.0, 64.0, 80.0, 88.0, 96.0, 112.0, and 120.0 ms for T_2. The ^{1}H-^{15}N NOEs were measured by recording the signal intensities in two experiments, one with a series of proton presaturation pulses and one with the presaturation period replaced by a delay of equal length (2.9 seconds). The T_2 data set was acquired using a ^{15}N 90° pulse width of 40.0 μs with a spacing of 500 μs between 180° pulses in the CPMG pulse train. The data were analyzed by measuring the peak intensities as a function of the variable relaxation delay. These were fitted, in the case of T_1 and T_2, to a decaying exponential, $I(t) = I_o\exp(-t/T_i)$ for each site i, using the conjugate gradient minimization technique.[46] ^{1}H-^{15}N NOE values were calculated from the intensity ratio of the spectrum obtained with presaturation to that obtained without presaturation modified by a correction factor that takes into account incomplete magnetization recovery during the recovery period.[47]

Protein Data Bank accession codes

The *A. fulgidus* SRP19 coordinates have been deposited in the RCSB Protein Data Bank under accession codes 1KVV and 1KVN for the energy-minimized average and the ensemble of accepted structures, respectively.

Acknowledgments

We gratefully acknowledge Frank Delaglio for the NMR processing package nmrPipe, Dan Garrett for the NMR data analysis package PIPP, Ad Bax for the IPAP-HSQC pulse program and the RDC analysis package PALES, Nico Tjandra and Marius Clore for the X-PLOR routines that enabled refinement of the structures against the experimental residual dipolar coupling data, and Zhanyong Shu, who assisted in the measurement and analysis of the backbone relaxation parameters. This work was supported by NIH grants GM49034 to C.Z. and RR13879 to A.P.H. and Robert A. Welch Foundation grant AQ-1413 to A.P.H.

Based on the close similarity between structures calculated with and without the RDC restraints, only those calculated from the NOE, dihedral, and RDC restraints have been deposited with the RCSB Protein Data Bank (energy-minimized average PDB code 1KVV; ensemble of accepted structures PDB code 1KVN).

References

1. Keenan, R. J., Freymann, D. M., Stroud, R. M. & Walter, P. (2001). The signal recognition particle. *Annu. Rev. Biochem.* **70**, 755-775.
2. Gorodkin, J., Knudsen, B., Zwieb, C. & Samuelsson, T. (2001). SRPDB (signal recognition particle database). *Nucl. Acids Res.* **29**, 169-170.
3. Larsen, N. & Zwieb, C. (1991). SRP-RNA sequence alignment and secondary structure. *Nucl. Acids Res.* **19**, 209-215.
4. Bhuiyan, S., Gowda, K., Hotokezaka, H. & Zwieb, C. (2000). Assembly of archaeal signal recognition particle from recombinant components. *Nucl. Acids Res.* **28**, 1365-1373.
5. Birse, D. E., Kapp, U., Strub, K., Cusack, S. & Aberg, A. (1997). The crystal structure of the signal recognition particle *Alu* RNA binding heterodimer, SRP9/14. *EMBO J.* **16**, 3757-3766.
6. Weichenrieder, O., Wild, K., Strub, K. & Cusack, S. (2000). Structure and assembly of the Alu domain of the mammalian signal recognition particle. *Nature,* **408**, 167-173.
7. Wild, K., Weichenrieder, O., Leonard, G. A. & Cusack, S. (1999). The 2 Å structure of helix 6 of the human signal recognition particle RNA. *Struct. Fold. Des.* **7**, 1345-1352.
8. Schmitz, U., Behrens, S., Freymann, D. M., Keenan, R. J., Lukavsky, P., Walter, P. & James, T. L. (1999).

Structure of the phylogenetically most conserved domain of SRP RNA. *RNA,* **5**, 1419-1429.
9. Jovine, L., Hainzl, T., Oubridge, C., Scott, W., Li, J., Sixma, T., Wonacott, A. *et al*. (2000). Crystal structure of the Ffh and EF-G binding sites in the conserved domain Iv of *Escherichia coli* 4.5S RNA. *Struct. Fold Des.* **8**, 527-540.
10. Keenan, R. J., Freymann, D. M., Walter, P. & Stroud, R. M. (1998). Crystal structure of the signal sequence binding subunit of the signal recognition particle. *Cell,* **94**, 181-191.
11. Clemons, W. M., Jr, Gowda, K., Black, S. D., Zwieb, C. & Ramakrishnan, V. (1999). Crystal structure of the conserved subdomain of human protein SRP54 M at 2.1 Å resolution: evidence for the mechanism of signal peptide binding. *J. Mol. Biol.* **292**, 697-705.
12. Batey, R. T., Rambo, R. P., Lucast, L., Rha, B. & Doudna, J. A. (2000). Crystal structure of the ribonucleoprotein core of the signal recognition particle. *Science,* **287**, 1232-1239.
13. Lingelbach, K., Zwieb, C., Webb, J. R., Marshallsay, C., Hoben, P. J., Walter, P. & Dobberstein, B. (1988). Isolation and characterization of a cDNA clone encoding the 19 kDa protein of signal recognition particle (SRP): expression and binding to 7SL RNA. *Nucl. Acids Res.* **16**, 9431-9442.
14. Zwieb, C. (1991). Interaction of protein SRP19 with signal recognition particle RNA lacking individual RNA helices. *Nucl. Acids Res.* **19**, 2955-2960.
15. Zwieb, C. (1992). Recognition of a tetranucleotide loop of signal recognition particle RNA by protein SRP19. *J. Biol. Chem.* **267**, 15650-15656.
16. Zwieb, C. (1994). Site-directed mutagenesis of signal recognition particle RNA: identification of the nucleotides in helix 8 required for interaction with protein SRP19. *Eur. J. Biochem.* **222**, 885-890.
17. Chittenden, K., Black, S. & Zwieb, C. (1994). Systematic site-directed mutagenesis of protein SRP19: identification of the residues essential for binding to signal recognition particle RNA. *J. Biol. Chem.* **269**, 20497-20502.
18. Black, S. D., Gowda, K., Chittenden, K., Walker, K. P., III & Zwieb, C. (1997). Identification of an RNA-binding-loop in the N-terminal region of signal-recognition-particle protein SRP19. *Eur. J. Biochem.* **245**, 564-572.
19. Wild, K., Sinning, I. & Cusack, S. (2001). Crystal structure of an early protein-RNA assembly complex of the signal recognition particle. *Science,* **294**, 598-601.
20. Pakhomova, O., Cui, Y., Zwieb, C. & Hinck, A. (2001). Sequence-specific ^{1}H, ^{13}C and ^{15}N signal assignments and secondary structure of *Archaeoglobus fulgidus* SRP19. *J. Biomol. NMR,* **20**, 187-188.
21. Hinck, A. P., Markus, M. A., Huang, S., Grzesiek, S., Kustanovich, I., Draper, D. E. & Torchia, D. A. (1997). The RNA binding domain of ribosomal protein L11: three-dimensional structure of the RNA-bound form of the protein and its interaction with 23S rRNA. *J. Mol. Biol.* **274**, 101-113.
22. Billeter, M., Guntert, P., Luginbuhl, P. & Wuthrich, K. (1996). Hydration and DNA recognition by homeodomains. *Cell,* **85**, 1057-1065.
23. Wikstrom, A., Berglund, H., Hambraeus, C., van den Berg, S. & Hard, T. (1999). Conformational dynamics and molecular recognition: backbone dynamics of the estrogen receptor DNA-binding domain. *J. Mol. Biol.* **289**, 963-979.
24. McGuire, A. M., Matsuo, H. & Wagner, G. (1998). Internal and overall motions of the translation factor eIF4E: cap binding and insertion in a CHAPS detergent micelle. *J. Biomol. NMR,* **12**, 73-88.
25. Eberhardt, E. S., Loh, S. N., Hinck, A. P. & Raines, R. T. (1992). Solvent effects on the energetics of prolyl peptide bond isomerization. *J. Am. Chem. Soc.* **114**, 5437-5439.
26. Wishart, D. S. & Sykes, B. D. (1994). The ^{13}C chemical-shift index: a simple method for the identification of protein secondary structure using ^{13}C chemical shift data. *J. Biomol. NMR,* **4**, 171-180.
27. Brünger, A. T. (1992). *X-PLOR Manual Version 3.1: A System for X-RAY Crystallography and NMR*, Yale University, New Haven CT.
28. Clore, G. M., Gronenborn, A. M. & Tjandra, N. (1998). Direct structure refinement against residual dipolar couplings in the presence of rhombicity of unknown magnitude. *J. Magn. Reson.* **131**, 159-162.
29. Chittenden, K., Gowda, K., Black, S. D. & Zwieb, C. (1997). Interaction of rice and human SRP19 polypeptides with signal recognition particle RNA. *Plant Mol. Biol.* **34**, 507-515.
30. Oubridge, C., Ito, N., Evans, P. R., Teo, C. H. & Nagai, K. (1994). Crystal structure at 1.92 Å resolution of the RNA-binding domain of the U1A spliceosomal protein complexed with an RNA hairpin. *Nature,* **372**, 432-438.
31. Burd, C. & Dreyfuss, G. (1994). Conserved structures and diversity of functions of RNA-binding proteins. *Science,* **265**, 615-621.
32. Goldgur, Y., Mosyak, L., Reshetnikova, L., Ankilova, V., Lavrik, O., Khodyreva, S. & Safro, M. (1997). The crystal structure of phenylalanyl-tRNA synthetase from thermus thermophilus complexed with cognate $tRNA^{Phe}$. *Structure,* **5**, 59-68.
33. Zwieb, C. (1991). A basic region neighboring the lysine-rich C terminus of protein SRP19 is required for binding to signal recognition particle RNA. *Biochem. Cell Biol.* **69**, 649-654.
34. Rose, M. A. & Weeks, K. M. (2001). Visualizing induced fit in early assembly of the human signal recognition particle. *Nature Struct. Biol.* **8**, 515-520.
35. Draper, D. E. (1999). Themes in RNA-protein recognition. *J. Mol. Biol.* **293**, 255-270.
36. Nelson, R. M. & Long, G. L. (1989). A general method of site-specific mutagenesis using a modification of the *Thermus aquaticus* polymerase. *Anal. Biochem.* **180**, 147-151.
37. Garrett, D. S., Powers, R., Gronenborn, A. M. & Clore, G. M. (1991). A common sense approach to peak picking in two-, three-, and four-dimensional spectra using automatic computer analysis of contour diagrams. *J. Magn. Res.* **95**, 214-220.
38. Cornilescu, G., Delaglio, F. & Bax, A. (1999). Protein backbone angle restraints from searching a database for chemical shift and sequence homology. *J. Biomol. NMR,* **13**, 289-302.
39. Sass, H. J., Musco, G., Stahl, S. J., Wingfield, P. T. & Grzesiek, S. (2000). Solution NMR of proteins within polyacrylamide gels: diffusional properties and residual alignment by mechanical stress or embedding of oriented purple membranes. *J. Biomol. NMR,* **18**, 303-309.
40. Ottiger, M., Delaglio, F. & Bax, A. (1998). Measurement of *J* and dipolar couplings from simplified two-dimensional NMR spectra. *J. Magn. Reson.* **131**, 373-378.

41. Nilges, M., Clore, G. M. & Gronenborn, A. M. (1988). Determination of three-dimensional structures of proteins from interproton distance data by hybrid distance geometry-simulated annealing calculations. *FEBS Letters,* **229**, 317-324.
42. Suri, A. K. & Levy, R. M. (1993). Estimation of interatomic distances in proteins from NOE spectra at longer mixing times using an empirical two-spin equation. *J. Magn. Res. ser. B,* **101**, 320-324.
43. Suri, A. K. & Levy, R. M. (1995). A relaxation-matrix analysis of distance-constraint ranges for NOEs in proteins at long mixing times. *J. Magn. Res. ser. B,* **106**, 24-31.
44. Zweckstetter, M. & Bax, A. (2000). Prediction of sterically induced alignment in a dilute liquid crystalline phase: aid to protein structure determination by NMR. *J. Am. Chem. Soc.* **122**, 3791-3792.
45. Kay, L. E., Nicholson, L. K., Delaglio, F., Bax, A. & Torchia, D. A. (1992). Pulse sequences for removal of the effects of cross correlation between dipolar and chemical-shift anisotropy relaxation mechanisms on the measurement of heteronuclear T1 and T2 values in proteins. *J. Magn. Reson.* **97**, 359-375.
46. Press, W. H., Flannery, B. P., Teukolsky, S. A. & Vetterling, W. T. (1988). *Numerical Recipes in C,* Cambridge University Press, Cambridge, UK.
47. Grzesiek, S. & Bax, A. (1993). The importance of not saturating H_2O in protein NMR: application to sensitivity enhancement and NOE measurements. *J. Am. Chem. Soc.* **115**, 12593-12594.
48. Kabsch, W. & Sander, C. (1983). Dictionary of protein secondary structure: pattern recognition of hydrogen-bonded and geometrical features. *Biopolymers,* **22**, 2577-2637.
49. Koradi, R., Billeter, M. & Wuthrich, K. (1996). MOLMOL: a program for display and analysis of macromolecular structures. *J. Mol. Graph.* **14**, 51-55.
50. Carson, M. (1997). RIBBONS. *Methods Enzymol.* **277**, 493-505.
51. Nicholls, A., Sharp, K. A. & Honig, B. (1991). Protein folding and association: insights from the interfacial and thermodynamic properties of hydrocarbons. *Proteins: Struct. Funct. Genet.* **11**, 281-296.
52. Laskowski, R. A., MacArthur, M. W., Moss, D. S. & Thornton, J. M. (1993). PROCHECK: a program to check the stereochemical quality of protein structures. *J. Appl. Crystallog.* **26**, 283-291.

Edited by D. Draper

(Received 4 September 2001; received in revised form 4 January 2002; accepted 9 January 2002)